HHS Public Access

Author manuscript

Magn Reson Med. Author manuscript; available in PMC 2014 November 02.

Published in final edited form as:

Magn Reson Med. 2014 March ; 71(3): 1221–1230. doi:10.1002/mrm.24763.

Detection of *in vivo* enzyme activity with catalyCEST MRI

Byunghee Yoo[1], **Vipul R. Sheth**[2], **Christine M. Howison**[3], **Matthew J. K. Douglas**[4], **Carlos T. Pineda**[4], **Erin A. Maine**[4], **Amanda F. Baker**[4,5], and **Mark D. Pagel**[4,6,7]

[1] MGH/MIT/HMS Athinoula A. Martinos Center for Biomedical Imaging, Massachusetts General Hospital and Harvard Medical School, Boston, MA

[2] Department of Biomedical Engineering, Case Western Reserve University, Cleveland OH

[3] Arizona Research Labs, University of Arizona, Tucson AZ

[4] University of Arizona Cancer Center, Tucson AZ

[5] Hematology/Oncology Section, College of Medicine, University of Arizona, Tucson AZ

[6] Department of Biomedical Engineering, University of Arizona, Tucson AZ

[7] Department of Chemistry and Biochemistry, University of Arizona, Tucson AZ

Abstract

Purpose—CatalyCEST MRI compares the detection of an enzyme-responsive CEST agent with the detection of an unresponsive “control” CEST agent that accounts for other conditions that influence CEST. The purpose of this study was to investigate the feasibility of in vivo catalyCEST MRI.

Methods—CEST agents that were responsive and unresponsive to the activity of urokinase Plasminogen Activator (uPA) were shown to have negligible interaction with each other. A CEST-FISP MRI protocol was used to acquire MR CEST spectroscopic images with a Capan-2 pancreatic tumor model after intravenous injection of the CEST agents. A function of (super)-Lorentzian line shapes was fit to CEST spectra of a region-of-interest that represented the tumor.

Results—The CEST effects from each agent showed the same initial uptake into tumor tissues, indicating that both agents had the same pharmacokinetic transport rates. Starting five minutes after injection, CEST from the enzyme-responsive agent disappeared more quickly than CEST from the unresponsive agent, indicating that the enzyme responsive agent was being catalyzed by uPA while both agents also experienced net pharmacokinetic washout from the tumor.

Conclusion—CatalyCEST MRI demonstrates that dynamic tracking of enzyme-responsive and unresponsive CEST agents during the same in vivo MRI study is feasible.

Keywords

CEST MRI; contrast agents; enzyme activity; molecular imaging

Corresponding Author: Mark D. Pagel University of Arizona Cancer Center University of Arizona 1515 N Campbell Avenue Tucson, AZ 85724-5024 Tel: (520)-404-7049 mpagel@u.arizona.edu.

INTRODUCTION

Enzyme activities are important biomarkers for diagnosing and monitoring many disease states. For example, urokinase Plasminogen Activator (uPA) is a protease biomarker for pancreatic tumor invasion and metastases because it activates other proteases that degrade the extracellular matrix and vessel basement membranes in the solid tumor and normal tissues that surround the tumor (1,2). Also, uPA causes paracrine and autocrine signaling that promotes tumor growth (3). Because uPA is initially expressed as a pro-enzyme, expression assays may inadvertently detect the inactive form of this enzyme, while measuring uPA activity necessarily reports on active uPA enzyme.

Fluorescence imaging agents have been developed that can detect enzyme activities. For example, uPA can cleave a ZGGR peptidyl ligand attached to a 7-amino-4-methylcoumarin (AMC), which causes the AMC to become highly fluorescent (Fig. 1A) (4). In addition, a second “control” fluorescent agent that is unresponsive to uPA activity can be selectively detected at the same time and in the same tissue location as the uPA-responsive agent. This control agent can account for pharmacokinetics of the enzyme-responsive agent (assuming that the agents have identical pharmacokinetics), which improves the detection of enzyme activity.

In vivo fluorescence imaging suffers from interfering light scattering in tissue, which limits spatial image resolution and the tissue depth that may be interrogated. For comparison, magnetic resonance imaging (MRI) produces images of deep tissues with relatively high spatial resolution. MRI contrast agents have been developed that detect protease activities after cleavage of a peptidyl ligand causes the agents to change the T_1- or T_2-relaxation time of surrounding water molecules (5). However, selectively detecting two relaxation-based MRI contrast agents is challenging, which complicates the comparison of enzyme-responsive and unresponsive MRI contrast agents at the same time and in the same tissue location (6).

Chemical Exchange Saturation Transfer (CEST) agents are an alternative to relaxation-based MRI contrast agents (5). A frequency-selective radio frequency pulse can saturate the coherent magnetization of a proton on the CEST agent, and subsequent chemical exchange of the proton with a water proton transfers the saturation to water, which causes a decrease in net MRI signal from water (Fig. 2A). Paramagnetic CEST agents typically consist of a lanthanide chelate, and the lanthanide ion shifts the MR frequencies of the chelate to unique values, which facilitates the selective saturation of one CEST agent in a mixture of agents.

We have previously designed CEST agents that can detect enzyme activities in chemical solutions (7-10). For example, we designed a uPA-responsive CEST agent by replacing the AMC group of ZGGR-AMC with a lanthanide chelate (Fig. 1B) (10). Cleavage of the ZGGR peptidyl ligand by uPA in a chemical solution converted an amide to an amine on the chelate, which caused the disappearance of CEST from the agent (Fig. 2B). In our previous studies, we included a CEST agent in the same chemical solution, Yb-DOTA-Gly_4, which does not have a peptidyl ligand and therefore served as a control agent to improve the detection of uPA enzyme activity. The comparison of the uPA-responsive CEST agent with

an unresponsive CEST agent improved the detection of enzyme activity, because assigning the absence of the CEST effect from the responsive agent that "turns off" after enzyme activity would be daunting without also detecting the unresponsive agent that is "always on". We refer to the comparison of an enzyme-responsive CEST agent and an unresponsive CEST agent as "catalyCEST MRI".

The translation of catalyCEST MRI to *in vivo* studies requires CEST MRI methods with fast temporal resolution, sufficient sensitivity, and selective detection of two CEST effects. We have previously developed CEST-FISP MRI that provides fast temporal resolution for tracking the pharmacokinetics of CEST agents during *in vivo* studies (11). We have also employed Lorentzian and super-Lorentzian line shape fitting methods that can be used to selectively detect two CEST effects (12,13). We have also employed a methodology for determining when CEST reaches a statistically significant threshold for sufficiently sensitive detection (14). These past accomplishments used unresponsive CEST agents. In this report, we investigated whether these past accomplishments can be used with responsive and unresponsive CEST agents to translate catalyCEST MRI to *in vivo* studies.

METHODS

Chemical Synthesis

The CEST agents, ZGGR-α-amino-(Tm-DOTA) (Fig. 1B) and Eu-DOTA-Gly_4 (Fig. 1C), were synthesized using previously reported methods (10,15). These products were characterized using electrospray mass spectrometry and were found to match previously reported results. The concentrations of ZGGR-α-amino-(Tm-DOTA) and Eu-DOTA-Gly_4 were confirmed using inductively coupled mass spectrometry.

CEST MRI protocol

MRI studies were conducted with a pre-clinical Bruker Biospec MRI scanner operating at 7.05 T (300 MHz) magnetic field strength and processed using ParaVision 5.1 software. The temperature of the magnet bore was calibrated by measuring the separation of resonances of neat methanol between 25°C and 40°C to ensure that phantom studies and *in vivo* studies were both conducted at 37°C (16). A CEST-FISP acquisition protocol was used for all CEST MRI studies (11). Selective saturation was applied using a series of Gaussian-shaped pulses with a 300 Hz bandwidth and 10 μT power for 4.714 seconds. FISP acquisition parameters included TR: 2.33 msec; TE: 1.16 msec; excitation flip angle: 60°; number of averages: 1; matrix: 64×64; field of view: 4×4 cm; in-plane spatial resolution: 625×625 μm; slice thickness: 1 mm. The temporal resolution of acquiring one image with one selective saturation frequency was 5.10 seconds.

Some CEST spectra contained spikes that were similar to "salt and pepper" noise that can complicate signal analyses in many types of engineering protocols (17). The CEST spectra were median filtered to remove the interference of these spikes during the fitting process. The median filter substituted the value of each data point with median value of a 3-point range about the data point. The filtering affected the center point of the direct saturation of

water in the CEST spectrum, but this original point was restored in the spectrum after filtering.

CEST MRI studies of chemical solutions

Mixtures of both contrast agents were prepared at identical concentrations for both agents. The CEST MRI protocol listed above was used to acquire a series of 101 images with selective saturation from 100 to −100 ppm to investigate the responsiveness of both agents to uPA activity (Fig. 2). A series of 31 images with selective saturation from 200 to −200 ppm was acquired to assess the dependence of CEST on concentration for each agent (Fig. 3). Due to the T1 relaxivity of Tm(III), the water MR signal increased with increasing concentration in each CEST-FISP image because FISP images experience T1-weighting. The water MR signal also changed as a function of saturation frequency. The scale of the images at different concentrations was adjusted so that the 25 mM sample with saturation applied at 200 ppm was considered to have 100% signal. All CEST MR images were acquired at 37°C. To obtain a CEST spectrum from these images, a Region Of Interest (ROI) was manually selected for each chemical solution to be evaluated.

A model function of three Lorentzian lines (Eq. [1], without the fourth term for the super-Lorentzian line shape, was fit to each CEST spectrum using customized routines developed for Matlab R2009B (Mathworks Inc., Natick, MA) (12). A CEST effect of 2√2 was considered to have a 95% probability that the CEST effect was real (14). CEST effects that reached this threshold of sensitivity were evaluated using a Hanes-Woolf-like linear analysis method that is based on a two-pool model in which the two pools represent water and one agent (18).

$$1-\frac{M_s}{M_0}= \frac{A_1 w_1}{\pi\left[(sf-\omega_1)^2+w_1^2\right]}+\frac{A_2 w_2}{\pi\left[(sf-\omega_2)^2+w_2^2\right]}+\frac{A_3 w_3}{\pi\left[(sf-\omega_3)^2+w_3^2\right]} + \frac{A_4}{\pi w_4}\sqrt{\frac{2}{\pi}}\int_0^{\pi/2} d\theta\, sin\theta \frac{1}{|3cos^2\theta-1|} exp\left\{-2\left[\frac{2(sf-\omega_4)}{w_4|3cos^2\theta-1|}\right]^2\right\} \quad (1)$$

where

A1,2,3,4 : the area of the Lorentzian line shape

w1,2,3,4 : the line width at half height of the Lorentzian line shape

ω1,2,3,4 : the maximum of the Lorentzian line shape

Cell Culture

Panc-1, Su86.86, Capan-2, and HPAF-II pancreatic cancer cells (American Type Culture Collection, Manassas, VA) were maintained in the recommended tissue culture media for each cell type, supplemented with 10% fetal bovine serum (FBS), 500 U/mL penicillin, and 5000 U/mL streptomycin. Cells were tested for mycoplasma contamination on a quarterly basis using the MycoAlert mycoplasma detection assay kit (Lonza Group Ltd., Basel, Switzerland) and found to be negative. Cells were grown in 5% CO_2 at 37°C in a humidified tissue culture incubator or exposed to 1.0% humidified oxygen concentration in nitrogen at

37°C in an Invivo Hypoxia Workstation 400 with a Ruskinn hypoxic gas mixer (Biotrace International, Cincinnati, OH).

In vivo tumor model

All *in vivo* studies were conducted according to approved procedures of the Institutional Animal Care and Use Committee of the University of Arizona. A mouse model was prepared by injecting 1.0 M Capan-2 tumor cells in 0.5 mL of 50% Matrigel into the right lower flank of 10 female Severe Combined Immune Deficiency (SCID) mice that were 6 weeks old. CEST MR studies were conducted when the subcutaneous tumor reached a size greater than 4 mm in diameter.

uPA Optical Absorbance Assay

The total uPa activity was analyzed using the PAI Activity Assay Kit (ECM610 Kit, Millipore, Inc., Billerica, MA). A linear calibration was constructed by preparing the substrate at the manufacturer's recommended concentration, and measuring colorimetric absorbance two hours after adding human urine uPA provided with the kit. The amount of uPa was varied between 0.625 and 10 Units. A Synergy 2 microplate reader (Biotek Instruments Inc., Winooski, VA) was used to monitor absorbance at 405 nm. Paired media samples without chromogenic substrate added were used for subtracting background absorbance. The absorbance of the uncleaved chromogenic substrate is unknown. However, our study evaluated changes in absorbances between samples and over time, which cancels any potential systematic error due to absorbance by uncleaved agent. To ensure that this assay quantified enzyme activity, the initial rate of substrate cleavage was monitored as a function of substrate concentration and the results were analyzed using a Lineweaver-Burk plot. After developing the assay, uPA activity was measured in experimental samples following two hours of incubation with the substrate. The amount of uPA activity in each experimental sample was determined from the calibration curve and normalized to total protein per well. The total protein content was measured using a 660 nm Protein Assay kit (Thermo Scientific, Rockford, IL).

For the determination of *in vitro* uPa activity, cells were seeded at 250,000 cells per 100 mm plate in 3 mL of media supplemented with 10% FBS. Cells were allowed to attach overnight and fresh media was added and collected after 48 hrs. Cells were tested with the uPA assay to identify the cell type with the highest activity of uPA.

For the determination of *in vivo* uPA activity, Capan-2 tumors were harvested from mice after euthanasia with CO_2 asphyxiation or with i.p. administration of 0.2 mL of pentobarbitol. Following harvesting, 250 mg of tumor sample was placed into a cryovial with 1 mL of 1x assay buffer from the uPA Activity Assay Kit. Samples were homogenized with a handheld Powergen homogenizer (Fisher Scientific) and sonicated. The sonication may have caused a decrease in enzyme activity (19). However, care was taken to sonicate each sample with the same amplitude and duration, so that sonication would not affect the relative comparisons of enzyme activities between the tissues. Following centrifugation at 2,000 g for 10 minutes at room temperature, the supernatant was removed and used in the uPA assay. In addition, blood was collected from the mice via cardiac puncture, the plasma

was isolated via centrifugation at 2,000 g for 10 minutes at room temperature, and the supernatant was used in the uPA assay. Four mice were tested with the uPA assay to establish that the *in vivo* tumor tissue had high uPA activity. The 10 mice that were tested with CEST MRI were also tested with the uPA assay to confirm high uPA activity in tumor tissues.

In vivo CEST MRI

Each mouse was anesthetized with 1.5-2.5% isoflurane delivered in 1 L/min oxygen gas ventilation. A 27 g catheter was inserted in the tail vein to facilitate an injection of contrast agents. The mouse was then secured to a customized MRI-compatible cradle, probes for monitoring rectal temperature and respiration were connected to the mouse, and core body temperature was regulated at 37.0 ± 0.2°C using an automated feedback loop between the temperature probe and an air heater (SA Instruments, Inc., Stony Brook, NY). Respiration gating was not used, because the tumor was located on the lower flank, and the flank was immobilized when the mouse was secured to the cradle. A 100 μL mixture of 12.5 mM of Eu-DOTA-Gly_4 and 50 mM of ZGGR-α-amino-(Tm-DOTA) was injected i.v. through a tail vein catheter, which delivered 0.05 mmol/Kg of Eu-DOTA-Gly_4 and 0.2 mmol/Kg of ZGGR-α-amino-(Tm-DOTA) to the mouse. The relative concentrations of each agent were chosen based on the greater CEST sensitivity for Eu-DOTA-Gly_4 relative to ZGGR-α-amino-(Tm-DOTA). The mixture was slowly injected during 30 seconds to avoid excessive backpressure in the catheter and tail vein. *In vivo* CEST MR images were then acquired. At the conclusion of the MRI scan, the mouse was removed from the MRI magnet and cradle and allowed to recover before euthanasia, to ensure that the contrast agents did not create acute toxicity.

Using the CEST MRI protocol listed above, series of 21 images were acquired, which required 1.8 minutes to acquire. The saturation frequencies were acquired in an order of +80, +70, +57, +54, +51, +48, +40, +30, +10, +5, 0, −5, −10, −30, −40, −48 −51, −54, −57, −70, and −80 ppm, relative to the average MR frequency of the tumor that was set to 0 ppm. The average MR frequency of the bladder differed from the average MR frequency of the tumor by approximately +3 ppm due to B_0 magnetic field inhomogeneity. A region of interest representing muscle tissue was selected near the tumor to minimize the effects of B_0 inhomogeneity when evaluating muscle. Regardless of B_0 inhomogeneities, the same saturation frequencies relative to the average MR frequency of the tumor region were used throughout the volume of the mouse.

Five mice were scanned at 1.8, 3.6, 5.4, 7.2, 9.0, and 10.8 minutes, and five additional mice were scanned at 3.0, 6.0, 9.0, 12.0, 15.0, and 18.0 minutes to improve temporal sampling. Parametric maps of the spatial distribution of CEST effects, known as CEST maps, were generated by subtracting the image acquired at a saturation frequency from the average image acquired with saturation at +80 and −80 ppm, and then normalized to the amplitude of the average image acquired with saturation at +80 and −80 ppm. To obtain a CEST spectrum of the tumor, bladder, or muscle, a ROI was manually selected in the CEST maps for each tissue to be evaluated. A model function of three Lorentzian line shapes and a super-Lorentzian line shape (Eq. [1]) were fit to each CEST spectrum using Matlab R2009B

(Mathworks Inc., Natick, MA) (13). The maximum of the Lorentzian line shape (i.e., the chemical shift of the direct saturation of water or the CEST peak) was a fitted parameter, so that this analysis method automatically compensated for B_0 inhomogeneity in the bladder and muscle relative to the tumor. Furthermore, the Lorentzian and super-Lorentzian line shape fittings were dependent on multiple points in the CEST spectrum, which compensated for the relatively sparse number of points in each CEST spectrum. The Lorentzian line shapes were used to account for CEST from both agents and the direct saturation of water, and the super-Lorentzian line shape was used to account for endogenous magnetization transfer effects. A CEST effect of $2\sqrt{2}$ was considered to have a 95% probability that the CEST effect was real (14).

RESULTS

The CEST agents ZGGR-α-amino-(Tm-DOTA) and Eu-DOTA-Gly_4, were synthesized using previously reported methods, and concentrations were confirmed using ICP-MS (10,15). ZGGR-α-amino-(Tm-DOTA) produced a CEST effect at −54.1 ppm, which disappeared after incubation with uPA (Fig. 2). Because the disappearance of a signal may be difficult to interpret, a CEST agent that is unresponsive to uPA activity, Eu-DOTA-Gly_4, was also included in the sample. CEST at +53.9 ppm from Eu-DOTA-Gly_4 did not change after adding uPA. A high salt content in the chemical samples compromised the “match” of the transceiver coil and increased the bandwidth of the saturation, which broadened the features in the CEST spectra.

CEST MR images were acquired with a series of chemical solutions that ranged in concentration from 1.56 to 25 mM (Fig. 3A). Lorentzian line shapes were fit to these spectra, resulting in negligible residuals relative to the amplitude of each CEST effect (Fig. 3B). The concentration dependence of CEST for each agent in a mixture of both agents was fit with a Hanes-Woolf-like analysis method that is based on a two-pool model of chemical exchange between only one agent and water (Fig. 3C).The excellent fitting of each agent to a two-pool model (R^2 = 0.95 and 0.96) indicated the direct interaction of the two CEST agents was negligible.

To develop a pre-clinical model with high uPA enzyme activity, a panel of pancreatic tumor cell lines was tested *in vitro* for uPA activity. An assay was developed using a colorimetric kit, which showed excellent linearity between the optical absorbance signal and the concentration of uPA (R^2 = 0.96, Fig.4A). The Michaelis-Menten kinetics of uPA for cleaving this agent was analyzed to assess whether the assay reported on enzyme activity (Fig. 4B). The excellent linearity of a Lineweaver-Burk plot (R^2 = 0.94) confirmed that catalysis of the agent with uPA matched a Michaelis-Menten enzyme kinetics model. A panel of pancreatic tumor cells was grown under normoxic and hypoxic conditions, and the cell media was assayed for extracellular uPA activity (Fig. 4C). The Capan-2 cell line exhibited the greatest uPA activity under normoxic conditions and the second-greatest uPA activity under hypoxic conditions. Excised tumors from four mice with a subcutaneous Capan-2 xenograft tumor showed strong uPA activity while very low or no uPA activity was detected in mouse plasma, further confirming that this tumor model was appropriate for *in vivo* CEST MRI studies of extracellular uPA activity in tumor tissue (Fig. 4D).

A mixture of ZGGR-α-amino-(Tm-DOTA) and Eu-DOTA-Gly_4 was injected i.v. through a catheter inserted in a tail vein in 10 mice with a subcutaneous Capan-2 tumor. CEST-FISP MR images were acquired at selective saturation frequencies ranging from +80 to −80 ppm, and CEST maps were generated at each saturation frequency relative to the average of CEST images acquired at +80 and −80 ppm (Fig. 5A). The CEST map at 0 ppm showed an apparent CEST effect in the bladder, which was attributed to B_0 inhomogeneity between the bladder and the tumor. The CEST maps were used to generate CEST spectra that represented the tumor, bladder, and muscle (Fig. 5B). These spectra were fit with Lorentzian and super-Lorentzian line shapes to quantify CEST from each agent. The low residuals of the fitting process attested to the high quality of this analysis method (Fig. 5C). A CEST effect of 2.2% reached the 95% probability threshold that the CEST effects were real, based on image noise. All *in vivo* CEST effects measured in tumor tissue were above this threshold, except for a measured CEST effect of 1.2% for Eu-DOTA-Gly_4 measured just prior to injection, which therefore was considered to be insignificant.

Each CEST effect was found to increase in tumor tissues at equal rates during the first 5 minutes after injection, suggesting that the pharmacokinetics of the agents were identical (Fig. 6B). However, the CEST effect of ZGGR-α-amino-(Tm-DOTA) decreased more rapidly than CEST from Eu-DOTA-Gly_4 in tumor tissues after 5 minutes post-injection (Fig. 6C). This difference in the rates of CEST disappearance was attributed to cleavage of the peptidyl ligand of ZGGR-α-amino-(Tm-DOTA) by uPA. Subsequent *ex vivo* assays confirmed high uPA activity in the tumor tissues. For comparison, the increase and decrease of each CEST effect in the bladder and muscle was the same for both agents, which was expected because these tissues have no uPA activity (Fig. 6D) (1). All *in vivo* CEST effects measured in bladder and muscle tissues exceeded the 99% probability threshold at 3.6 minutes after injection. This delay in reaching a minimum concentration to generate a detectable CEST effect was expected for the bladder, due to the time required for filtration of agents through the kidney. This delay was also expected for the muscle, due to the lower vascular permeability in muscle tissue relative to tumors (20).

DISCUSSION

The CEST effects of ZGGR-α-amino-(Tm-DOTA) and Eu-DOTA-Gly_4 were detected at approximately −54 and +54 ppm. This symmetry about the water resonance was advantageous when comparing the CEST effects of the two exogenous agents. In particular, the endogenous MT effect was symmetrical at these chemical shifts, so that competition with MT equally affected CEST from both agents (21). Furthermore, T_{2ex} relaxation from Eu-DOTA-Gly_4 may cause line broadening of the water resonance (22). Yet this line broadening was symmetrical, so that these relaxation effects equally affect CEST from both agents. This advantage of symmetrical CEST effects was not realized in our previous report that compared CEST effects of ZGGR-α-amino-(Tm-DOTA) and Yb-DOTA-Gly_4 that has a chemical shift at −16 ppm.

The symmetry of the two CEST effects creates a disadvantage. A CEST effect is commonly measured by directly comparing the water signal amplitude in the CEST spectrum at symmetrical chemical shifts relative to the chemical shift of water, known as a MTR_{asym}

analysis, because one half of the CEST spectrum is not influenced by a CEST agent (23). However, a mixture of ZGGR-α-amino-(Tm-DOTA) and Eu-DOTA-Gly_4 generates CEST in both halves of the CEST spectrum, which obviates the MTR_{asym} analysis method. To overcome this problem, a function of three Lorentzian line shapes was fit to CEST spectra obtained from chemical solutions (Fig. 2, 3). To overcome the additional problem of endogenous MT effects, one super-Lorentzian line shape was added to this function to fit to CEST spectra obtained from *in vivo* studies (Fig. 5, 6). As an additional benefit, this fitting procedure accounted for small changes in chemical shifts that may be caused by B_0 inhomogeneities or changes in temperature or pH. Therefore, this demonstration emphasizes the merits of Lorentzian and super-Lorentzian line fitting for CEST analyses.

The CEST-FISP MRI protocol generated “MR CEST-spectroscopic images” in 1.8 minutes. This temporal resolution was sufficient to track the washout of the two CEST agents in the tumor tissue between 5 and 18 minutes after injection, while also tracking the faster decrease in CEST detection from ZGGR-α-amino-(Tm-DOTA) that was caused by uPA catalysis. This temporal resolution was also sufficient for tracking the pharmacokinetics of both agents in bladder and muscle tissues for as long as 18 minutes after injection. However, a 1.8-minute temporal resolution was only marginally sufficient for tracking the pharmacokinetic uptake of both agents during the first 3.6 minutes after injection. This marginal temporal resolution prompted us to test two sets of mice with different temporal frames to improve the analyses of *in vivo* pharmacokinetics, which strengthened the conclusions reached with only one set of temporal frames. This result demonstrated that fast temporal resolution is desirable for tracking responsive and unresponsive CEST agents. Reducing the number of saturation frequencies can improve temporal resolution of MR CEST spectroscopic imaging, although care must be taken to retain sufficient spectral resolution to accurately measure CEST effects (24).

For comparison, some other *in vivo* studies have compensated for slower temporal resolution by directly injecting a CEST agent into tissues (13,25-30). Although injections of agents directly into tissues can be useful for proof-of-concept with new contrast agents, other routes of administration are preferred for a truly non-invasive imaging method. As another comparison, some other *in vivo* studies with i.v. injections have used spin-echo or SWIFT MRI protocols that have temporal resolutions as fast as 36.6 seconds per image (22,31,32). At this rate, the acquisition of 21 images with different saturation frequencies to generate a MR CEST spectroscopic image in our study would have required 12.8 minutes, which is too slow to assess the pharmacokinetics of our CEST agents. Other *in vivo* studies have detected CEST agents using OPARACHEE MRI that directly saturates the water resonance, resulting in a temporal resolution as fast as 80 seconds (33,34). However, OPARACHEE MRI cannot selectively detect multiple CEST agents during a single MRI protocol, which is insufficient for catalyCEST MRI studies. Therefore, a CEST-FISP MRI protocol appears particularly suitable for in vivo catalyCEST MRI studies.

Other *in vivo* MRI studies with exogenous agents have been previously reported. Initial *in vivo* studies tracked the dynamic uptake of paramagnetic CEST agents in tumors by iteratively saturating a single MR frequency before and after injection (14,35,36). However, this methodology cannot account for B_0 inhomogeneity or changes in line broadening from

T_2 relaxation. Subsequent *in vivo* studies saturated MR frequencies that are symmetrical about the water resonance using single-point (22,25,31) or multipoint (26,30) MTR_{asym} analysis. Recent *in vivo* studies have acquired and evaluated a full CEST spectrum, which improves on these previous approaches (28-30,37,38). As shown in our current study, fitting (super)-Lorentzian line shapes to CEST spectra is a useful method for evaluating *in vivo* studies that employ MR CEST-spectroscopic imaging.

Using a statistical threshold was critical for validating the appearance of *in vivo* CEST effects with exogenous contrast agents. We used a well-known criterion for evaluating changes in MR signal (i.e., contrast) relative to invariant MR signal that represented image noise (39). Despite the reduction in MR signal obtained with FISP acquisition methods, our CEST-FISP images still had high signal-to-noise, so that the Rician noise distribution could be approximated as a Gaussian noise distribution for assessing this probability threshold. Other statistical criteria have been used to validate other MR image contrast changes, particularly for fMRI studies. Therefore, additional methods for evaluating future *in vivo* MR CEST spectroscopic imaging studies may be warranted.

Although these results indicated that the pharmacokinetics is the same for both agents, identical pharmacokinetics is not guaranteed. In particular, ZGGR-α-amino-(Tm-DOTA) possesses a +1 net charge and Eu-DOTA-Gly_4 possesses a −1 net charge, and this difference in charge may affect pharmacokinetics. To address this potential pitfall, future studies should couple both agents together. For example, past studies have shown that a CEST agent can be coupled together by conjugating them to a dendrimer, which may also deliver a payload of agent to the tumor tissue and therefore also improve in vivo CEST detection (36). During future studies that couple CEST agents, care should be taken to ensure that each coupled agent does not interfere with the CEST effect of the other agent, as demonstrated in Figure 2D.

Other protease enzymes in the tumor tissue may have cleaved ZGGR-α-amino-(Tm-DOTA) during the *in vivo* CEST MRI studies, because proteases are notoriously promiscuous (2). The selective detection of multiple promiscuous proteases can be improved by using multiple fluorescence agents to monitor multiple cleavage rates, which can be used to solve coupled kinetics equations. Similarly, the ability to selectively detect multiple CEST agents within *in vivo* tumor tissues may also be exploited in future studies to selectively detect multiple promiscuous proteases. This study demonstrates that *in vivo* catalyCEST MRI with multiple CEST agents can be conducted to investigate these improvements. Furthermore, the catalytic efficiency of uPA for cleaving ZGGR-α-amino-(Tm-DOTA) within in vivo tumor tissues is unknown. Currently, in vivo enzyme kinetics studies are extremely difficult to perform. This study indicates that in vivo Michaelis-Menten kinetics studies may be feasible by serially performing non-invasive catalyCEST MRI studies with different substrate concentrations.

Finally, other catalyCEST agents have been designed that detect the catalytic activity of enzymes, including CEST agents that are catalyzed by protease (7,8,10,40), galactosidase (41,42) esterase (9), deaminase (43), and transglutaminase enzymes (44). These catalyCEST agents have been studied in chemical solutions, and some examples have been studied with

in vitro conditions. Our study represents the first report of in vivo catalyCEST MRI, and therefore demonstrates that the translation of these other catalyCEST agents to in vivo studies may be feasible.

CONCLUSIONS

Monitoring the *in vivo* pharmacokinetics of two CEST agents that were simultaneously injected i.v. into a single mouse provided the ability to simultaneously track delivery and enzyme catalysis, which improved the analysis of enzyme activity in a tumor model. Using a CEST-FISP MRI protocol, a (super)-Lorentzian line shape fitting to CEST spectra, and a threshold for establishing that CEST detection was statistically significant, were important design criteria for this study. Together, the two CEST agents and CEST MRI acquisition & analysis methods used in this study have established catalyCEST MRI for detecting *in vivo* enzyme activity.

Acknowledgements

This work was supported in part NIH Grants R21CA133455-01 and RO1CA125627. V.R.S. was supported through the US Army Medical Research and Materiel Command under grant no. W81XWH-09-1-0053 and in part by the CWRU MSTP under NIH grant no. T32 GM007250.B.Y., A.F.B. and M.D.P. conceived and designed the study, analyzed the results, and wrote the manuscript. B.Y., V.R.S., and C.M.H. conducted the MRI experiments. B.Y., M.J.K.D., C.T.P. and E.A.M. conducted the optical absorbance assays for uPA activity.

References

1. Duffy MJ. Proteases as prognostic markers in cancer. Clin Cancer Res. 1996; 2:613–618. [PubMed: 9816210]
2. Koblinski JE, Ahram M, Sloane BL. Unraveling the role of proteases in cancer. Clinica Chimica Acta. 2000; 291:113–135.
3. Nguyen DH, Hussaini IM, Gonias SL. Binding of urokinase-type plasminogen activator to its receptor in MCF-7 cells activates extracellular signal-regulated kinase 1 and 2 which is required for increased cellular motility. J Biol Chem. 1998; 273:8502–8507. [PubMed: 9525964]
4. Laube F, Göhring B, Sann GH, Willhardt I. Cell surface antigens in renal tumour cells: detection by immunoluminescence and enzymatic analysis. Br J Cancer. 2001; 85:924–929. [PubMed: 11556847]
5. Yoo B, Pagel MD. An overview of responsive MRI contrast agents for molecular imaging. Front Biosci. 2007; 13:1733–1752. [PubMed: 17981664]
6. Martinez GV, Zhang X, García-Martín ML, Morse DL, Woods M, Sherry AD, Gillies RJ. Imaging the extracellular pH of tumors by MRI after injection of a single cocktail of T(1) and T(2) contrast agents. NMR Biomed. 2011; 24:1380–1391. [PubMed: 21604311]
7. Yoo B, Pagel MD. A PARACEST MRI contrast agent to detect enzyme activity. J Am Chem Soc. 2006; 128(43):14032–14033. [PubMed: 17061878]
8. Yoo B, Raam M, Rosenblum R, Pagel MD. Enzyme-responsive PARACEST MRI contrast agents: A new biomedical imaging approach for studies of the proteasome. Contrast Media Molec Imaging. 2007; 2:189–198. [PubMed: 17712869]
9. Li Y, Sheth VR, Liu G, Pagel MD. A self-calibrating PARACEST MRI contrast agent that detects esterase enzyme activity. Contrast Media Molec Imaging. 2011; 6:219–228. [PubMed: 21861282]
10. Yoo B, Sheth V, Pagel MD. An amine-derivatized, DOTA-loaded polymeric support for Fmoc Solid Phase Peptide Synthesis. Tet Lett. 2009; 50:4459–4462.
11. Shah T, Lu L, Dell K, Pagel MD, Griswold M, Flask CA. CEST-FISP: A Novel Technique for Rapid Chemical Exchange Saturation Transfer (CEST) MRI at 7T. Magn Reson Med. 2011; 65:432–437. [PubMed: 20939092]

12. Sheth VR, Liu G, Li Y, Pagel MD. Improved pH measurements with a single PARACEST MRI contrast agent. Contrast Media Molec Imaging. 2012; 7:26–34. [PubMed: 22344877]
13. Sheth VR, Li Y, Chen LQ, Howison CM, Flask CA, Pagel MD. Measuring in vivo tumor pHe with CEST-FISP MRI. Magn Reson Med. 2012; 67:760–768. [PubMed: 22028287]
14. Liu G, Ali MM, Yoo B, Griswold MA, Tkach JA, Pagel MD. PARACEST MRI with improved temporal resolution. Magn Reson Med. 2009; 61:399–408. [PubMed: 19165903]
15. Aime S, Barge A, Castelli DD, Fedeli F, Mortillaro A, Nielsen FU, Terreno E. Paramagnetic lanthanide(III) complexes as pH-sensitive chemical exchange saturation transfer (CEST) contrast agents for MRI applications. Magn Reson Med. 2002; 47:639–648. [PubMed: 11948724]
16. Van Geet AL. Calibration of the methanol and glycol nuclear magnetic resonance thermometers with a static thermistor probe. Anal Chem. 1968; 40:2227–2229.
17. Chan RH, Ho CW, Nikolova M. Salt-and-pepper noise removal by median-type noise detector and edge-preserving regularization. IEEE Trans Image Proc. 2005; 14:1479–1485.
18. Ali MM, Liu G, Shah T, Flask CA, Pagel MD. Using Two Chemical Exchange Saturation Transfer Magnetic Resonance Imaging Contrast Agents for Molecular Imaging Studies. Acc Chem Res. 2009; 42:915–924. [PubMed: 19514717]
19. Chambers LA. The influence of intense mechanical vibration on the proteolytic activity of pepsin. J Biol Chem. 1937; 117:639–649.
20. Delrue LJ, Casneuf V, Van Damme N, Blanckaert P, Peeters M, Ceelen WP, Duyck PCO. Assessment of neovascular permeability in a pancreatic tumor model using dynamic contrast-enhanced (DCE) MRI with contrast agents of different molecular weights. Magn Reson Mat Phys Biol Med. 2011; 24(4):225–232.
21. Li AX, Hudson RHE, Barrett JW, Jones CK, Pasternak SH, Bartha R. Four-Pool Modeling of Proton Exchange Processes in Biological Systems in the Presence of MRI–Paramagnetic Chemical Exchange Saturation Transfer (PARACEST) Agents. Magn Reson Med. 2008; 60:1197–1206. [PubMed: 18958857]
22. Soesbe TC, Togao O, Takahashi M, Sherry AD. SWIFT-CEST: A New MRI Method to Overcome T2 Shortening Caused by PARACEST Contrast Agents. Magn Reson Med. 2012; 68:816–821. [PubMed: 22213371]
23. Sun PZ, Jinyuan Zhou J, Sun W, Huang J, van Zijl PCM. Suppression of Lipid Artifacts in Amide Proton Transfer. Magn Reson Med. 2005; 54:222–225. [PubMed: 15968669]
24. Tee Y, Chappell MA, Xie J, Payne SJ. CEST Sensitivity Functions Based Sampling Schedule. Proc Intl Soc Mag Reson Med. 2011; 19:4491.
25. Liu G, Li Y, Sheth VR, Pagel MD. Imaging in vivo extracellular pH with a single PARACEST MRI contrast agent. Molec Imaging. 2012; 11:47–57. [PubMed: 22418027]
26. Flament J, Geffroy F, Medina C, Robic C, Mayer JF, Mériaux S, Valette J, Robert P, Port M, Le Bihan D, Lethimonnier F, Boumezbeur F. In vivo CEST MR imaging of U87 mice brain tumor angiogenesis using targeted LipoCEST contrast agent at 7 T. Magn Reson Med. 2012 in press. DOI: 10.1002/mrm.24217.
27. Chen LQ, Sheth VR, Howison CA, Kuo PH, Pagel MD. Measuring in vivo tumor pHe with a DIACEST MRI contrast agent. Proc Intl Soc Mag Reson Med. 2011; 19:315.
28. McVicar N, Li AX, Suchý M, Hudson RHE, Menon RS, Bartha R. Simultaneous in vivo pH and temperature mapping using a PARACEST-MRI contrast agent. Magn Reson Med. 2012 in press. DOI: 10.1002/mrm.24539.
29. Castelli DD, Dastrú W, Terreno E, Cittadino E, Mainini F, Torres E, Spadaro M, Aime S. In vivoMRI multicontrast kinetic analysis of the uptake and intracellular trafficking ofparamagnetically labeled liposomes. J Controlled Release. 2010; 144:271–279.
30. Liu G, Moake M, Har-el YE, Long CM, Chan KW, Cardona A, Jamil M, Walczak P, Gilad AA, Sgouros G, van Zijl PC, Bulte JW, McMahon MT. In vivo multicolor molecular MR imaging using diamagnetic chemical exchange saturation transfer liposomes. Magn Reson Med. 2012; 67:1106–1113. [PubMed: 22392814]
31. Chan KW, McMahon MT, Kato Y, Liu G, Bulte JW, Bhujwalla ZM, Artemov D, van Zijl PC. Natural D-glucose as a biodegradable MRI contrast agent for detecting cancer. Magn Reson Med. 2012; 68(6):1764–73. [PubMed: 23074027]

32. Liu G, Chan KW, Song X, Zhang J, Gilad AA, Bulte JW, van Zijl PC, McMahon MT. Normalized magnetization ratio (NOMAR) filtering for creation of tissue selective contrast maps. Magn Reson Med. 2013; 69(2):516–23. [PubMed: 22499503]
33. Vinogradov E, He H, Lubag A, Balschi JA, Sherry AD, Lenkinski RE. MRI Detection of Paramagnetic Chemical Exchange Effects in Mice Kidneys In vivo. Magn Reson Med. 2007; 58:650–655. [PubMed: 17899603]
34. Li AX, Suchy M, Li C, Gati JS, Meakin S, Hudson RHE, Menon RS, Bartha R. In vivo Detection of MRI-PARACEST Agents in Mouse Brain Tumors at 9.4 T. Magn Reson Med. 2011; 66:67–72. [PubMed: 21254213]
35. Ali MM, Yoo B, Pagel MD. Tracking the relative in vivo pharmacokinetics of nanoparticles with PARACEST MRI. Molec Pharmaceutics. 2009; 6(5):1409–1416.
36. Ali MM, Bhuiyan MPI, Janic B, Varma NRS, Mikkelsen T, Ewing JR, Knight RA, Pagel MD, Arbab AS. A nano-sized PARACEST-fluorescence imaging contrast agent facilitates & validates in vivo CEST MRI detection of glioma. Nanomed. 2012; 7(12):1827–1837.
37. Longo DL, Dastru W, Digilio G, Keupp J, Langereis S, Lanzardo S, Prestigio S, Steinbach O, Terreno E, Uggeri F, Aime S. Iopamidol as a Responsive MRI-Chemical Exchange Saturation Transfer Contrast Agent for pH Mapping of Kidneys: In vivo Studies in Mice at 7 T. Magn Reson Med. 2011; 65:202–211. [PubMed: 20949634]
38. Ferrauto G, Castelli DD, Terreno E, Aime S. In vivo MRI Visualization of Different Cell PopulationsLabeled with PARACEST Agents. Magn Reson Med. 2012 in press. DOI: 10.1002/mrm.24411.
39. Haake, EM.; Brown, RW.; Thompson, MR.; Venkatesan, R. Physical Principles and Sequence Design. John Wiley & Sons; New York: 1999. Magnetic Resonance Imaging.
40. Suchy M, Ta R, Li AX, Wojciechowski F, Pasternak SH, Bartha R, Hudson RHE. A paramagnetic chemical exchange-based MRI probe metabolized by cathepsin D: design, synthesis and cellular uptake studies. Org Biomolec Chem. 2010; 8(11):2560–2566.
41. Chauvin T, Durand P, Bernier M, Meudal H, Doan BT, Noury F, Badet B, Beloeil JC, Tóth E. Detection of enzymatic activity by PARACEST MRI: a general approach to target a large variety of enzymes. Angew Chem Int Ed. 2008; 47:4370–4372.
42. Chauvin T, Torres S, Rosseto R, Kotek J, Badet B, Durand P, Tóth E. Lanthanide(III) Complexes That Contain a Self-Immolative Arm: Potential Enzyme Responsive Contrast Agents for Magnetic Resonance Imaging. Chem Eur J. 2012; 18:1408–1418. [PubMed: 22213022]
43. Liu G, Liang Y, Bar-Shir A, Chan KWY, Galpoththawela CS, Bernard SM, Tse T, Yadav NN, Walczak P, McMahon MT, Bulte JWM, van Zijl PCM, Gilad AA. Monitoring Enzyme Activity Using a Diamagnetic Chemical Exchange Saturation Transfer Magnetic Resonance Imaging Contrast Agent. J Am Chem Soc. 2011; 133:16326–16329. [PubMed: 21919523]
44. Hingorani DV, Pagel MD. An enzyme-responsive PARACEST MRI contrast agent that “turns on” after catalysis. Proc Intl Soc Mag Reson Med. 2012; 20:486.

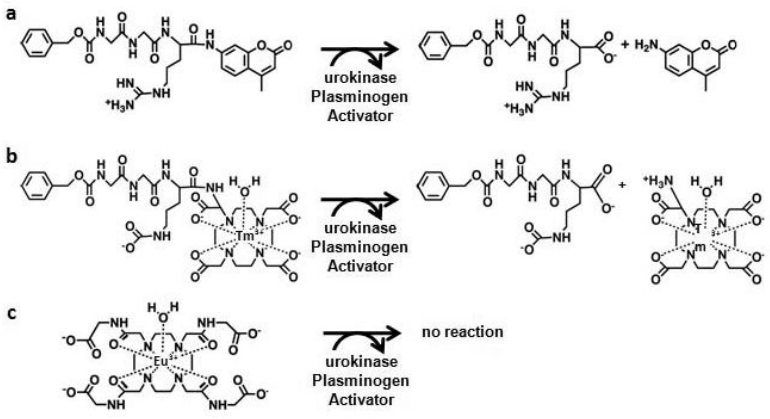

Figure 1.

Chemical structures of imaging contrast agents. a) The ZGGR peptide ligand is cleaved from the 7-amino-4-methylcoumarin (AMC) by urokinase Plasminogen Activator (uPA). The ligand-free AMC has bright fluorescence, which can be temporally monitored to detect uPA enzyme activity. b) ZGGR-α-amino-(Tm-DOTA) has the same design as ZGGR-AMC for detecting uPA activity. A water molecule fills the ninth coordinate site of the Tm-DOTA chelate. However, the CEST effect at −54 ppm from this agent originates from the amide nearest the Tm(III) ion. c) Eu-DOTA-Gly_4 does not contain a ZGGR peptide and is therefore unresponsive to uPA activity. A water molecule fills the ninth coordinate site of the Eu-DOTA chelate. The CEST effect at +54 ppm from this agent originates from the bound water molecule.

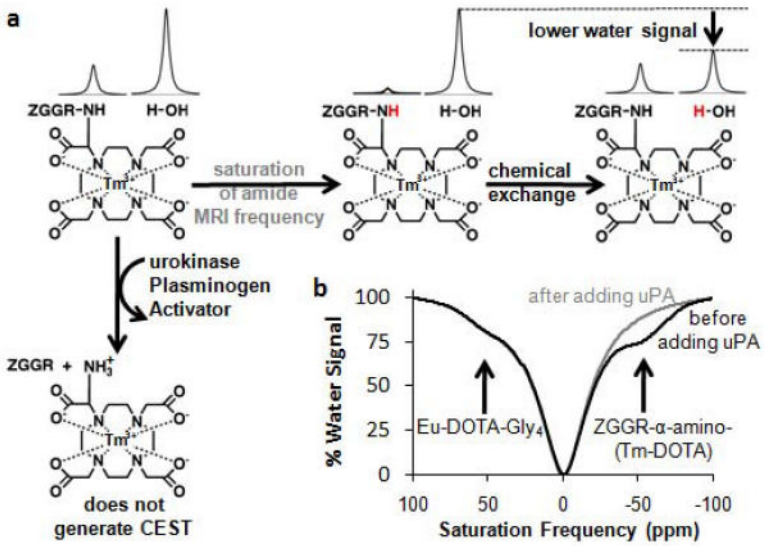

Figure 2.

Solution-state CEST MRI of two PARACEST agents. a) The horizontal reaction shows MR saturation of the amide proton of ZGGR-α-amino-(Tm-DOTA) (gray), followed by chemical exchange with water, which transfers the MR saturation to water and decreases the water signal. The vertical reaction shows cleavage of the ZGGR peptide from α-amino-(Tm-DOTA) by uPA, which converts an amide to an amine that does not generate CEST. b) ZGGR-α-amino-(Tm-DOTA) showed CEST with MR saturation at −54.1 ppm before adding uPA (black) but not after adding uPA (gray). A control agent, Eu-DOTA-Gly_4, showed no change in CEST at +53.9 ppm.

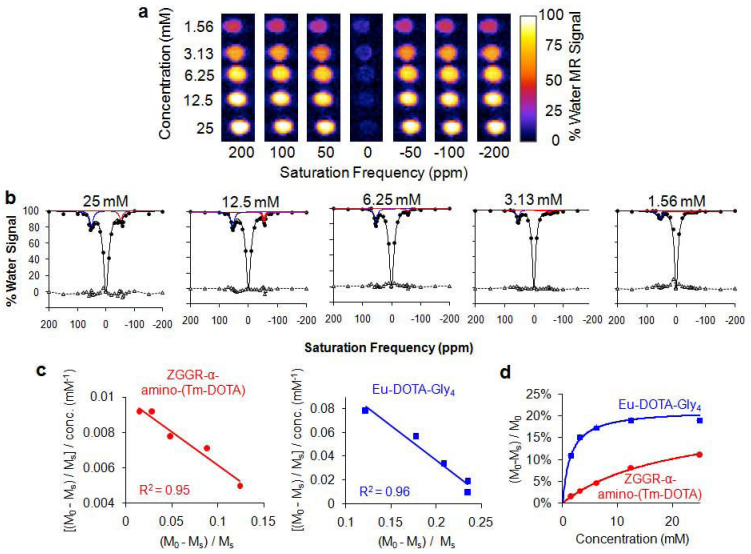

Figure 3.

Quantitative evaluation of the concentration dependence of CEST for each agent. a) Serially-diluted chemical solutions, with each solution containing both contrast agent at the same concentration, were used to acquire 31 CEST-FISP MR images with selective saturation ranging from +200 to −200 ppm. Only 7 of the 31 images are shown. b) A function of three Lorentzian line shapes was fit to each CEST spectrum to measure each CEST effect of ZGGR-α-amino-(Tm-DOTA) (red) and Eu-DOTA-Gly$_4$ (blue). Fitting residuals are shown as triangles with a dashed line. The residuals had a standard deviation ranging from 1.1% to 2.5% water signal for each fitting, which attested to the excellent quality of the fittings. c) The CEST results and concentrations were fit with a Hanes-Woolf-like linear analysis method based on a two-pool model of chemical exchange between only one agent and water. The excellent fitting indicated that each CEST effect can be approximated as a two-pool model, so that the direct interaction of the two CEST agents can be considered to be negligible. d) Based on results from the Hanes-like analysis method, the CEST effects of each PARACEST agent showed a typical correlation with concentration.

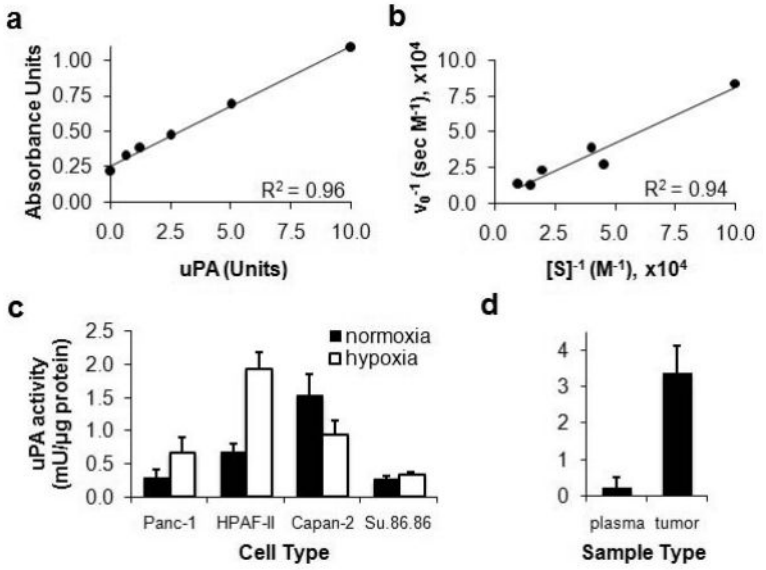

Figure 4.

Development of a pancreatic tumor model with high uPA activity. a) Total uPa activity was analyzed using the PAI Activity Assay Kit (ECM610 Kit, Millipore, Inc.) and a Synergy 2 microplate reader (Biotek Instruments Inc., Winooski, VA). Paired media samples without chromogenic substrate added were used for subtracting background absorbance. b) To ensure that enzyme concentration measured by this assay quantified enzyme activity, the initial rate of substrate cleavage was monitored as a function of substrate concentration and the results were analyzed using a Lineweaver-Burk plot. c) uPA activity was measured following two hours of incubation of the substrate with each cell type during *in vitro* studies conducted in normoxic and hypoxic conditions. The amount of uPa activity was normalized to total protein in each sample. Error bars represent the standard deviation of six trials for each cell type. d) The uPA activity was measured in blood plasma and homogenized tumor tissue. The amount of uPa activity in the samples was normalized to total protein in each sample. Error bars represent the standard deviation of results from four mice.

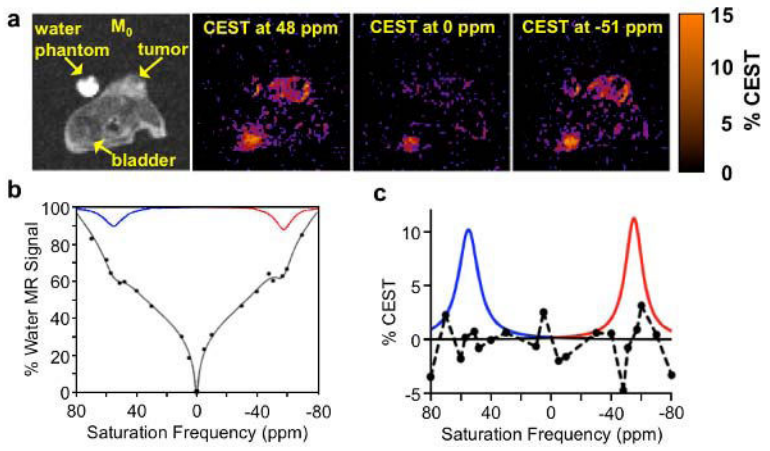

Figure 5.

In vivo CEST MRI of two PARACEST agents. a) A CEST image and CEST maps obtained at 3.6 minutes post-injection showed selective detection of each agent in the tumor and bladder. b) CEST spectra of the tumor were fit with Lorentzian and super-Lorentzian line shapes. The two Lorentzian line shapes corresponding to the CEST effects of the two agents are shown. c) CEST from each agent was quantified from each Lorentzian line shape. Residuals of the line shape fitting are shown as a dashed line.

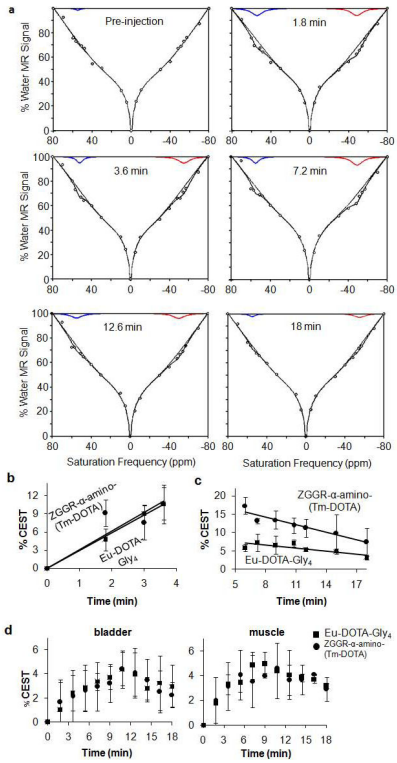

Figure 6.

CatalyCEST MRI. a) A function of three Lorentzian line shapes and one super-Lorentzian line shape was fit to each CEST spectrum (circles). The Lorentzian line shapes corresponding to ZGGR-α-amino-(Tm-DOTA) and Eu-DOTA-Gly_4 are shown, the sum of the four (super)-Lorentzian line shapes are also shown, and the sum of the super-Lorentzian line shape and the Lorentzian line shape of the direct saturation of water are also shown. b) Each agent showed the same initial tumor uptake rates, c) but the rates of CEST disappearance from the tumor were different for each agent. The faster CEST disappearance from ZGGR-α-amino-(Tm-DOTA) was attributed to uPA activity. d) The agents had the same pharmacokinetics in the bladder and muscle.